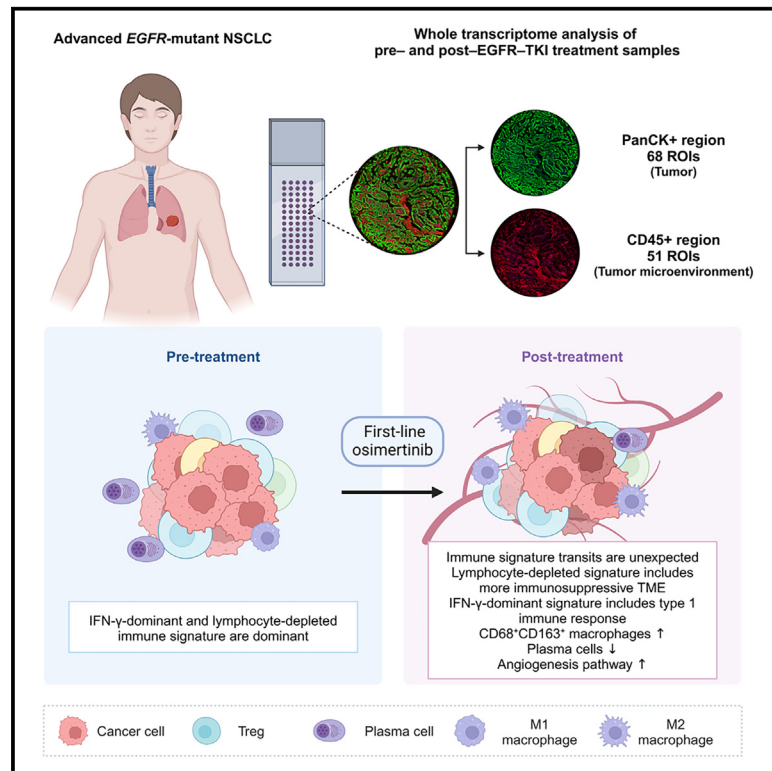**Article**

Remodeling of tumor microenvironments by EGFR tyrosine kinase inhibitors in *EGFR*-mutant non-small cell lung cancer

Graphical abstract

Authors

Soomin Kim, Jaemoon Koh,
Tae Min Kim, ..., Yoon Kyung Jeon,
Dong-Wan Kim, Dae Seog Heo

Correspondence

gabriel9@snu.ac.kr

In brief

Therapeutics; Microenvironment; Immune response; Cancer.

Highlights

- After EGFR-TKI treatment, tumor microenvironment becomes immunosuppressive

- Osimertinib treatment reduces immune cell infiltration and increases angiogenesis

- Immune signatures of *EGFR*-mutant NSCLC were IFN-γ-dominant and lymphocyte-depleted

- IFN-γ-dominant transit after EGFR-TKI facilitates response to ABCP treatment

CellPress

iScience

Article

Remodeling of tumor microenvironments by EGFR tyrosine kinase inhibitors in *EGFR*-mutant non-small cell lung cancer

Soomin Kim,[1,2,5] Jaemoon Koh,[3,5] Tae Min Kim,[1,4,6,*] Songji Oh,[1,2] Soyeon Kim,[1] Jeonghwan Youk,[1,4] Miso Kim,[1,4] Bhumsuk Keam,[1,4] Yoon Kyung Jeon,[1,2,3] Dong-Wan Kim,[1,2,4] and Dae Seog Heo[1,4]

[1]Cancer Research Institute, Seoul National University, Seoul, Republic of Korea
[2]Integrated Major in Innovative Medical Science, Seoul National University College of Medicine, Seoul, Republic of Korea
[3]Department of Pathology, Seoul National University Hospital, Seoul National University College of Medicine, Seoul, Republic of Korea
[4]Department of Internal Medicine, Seoul National University Hospital, Seoul National University College of Medicine, Seoul, Republic of Korea
[5]These authors equally contributed
[6]Lead contact
*Correspondence: gabriel9@snu.ac.kr
https://doi.org/10.1016/j.isci.2024.111736

SUMMARY

Patients with *EGFR* mutations exhibit immunosuppressive microenvironments, limiting responsiveness to immunotherapy. We used digital spatial profiling to analyze non-small cell lung carcinomas in 25 patients before and after EGFR tyrosine kinase inhibitor (TKI) treatment, including 14 patients treated with first-line osimertinib, focusing on CD45-positive immune regions and pan-cytokeratin-positive tumor regions. Osimertinib treatment resulted in altered angiogenic pathways and immune cell proportions, with reduced plasma cells (22.2%–11.7%; $p = 0.025$) and increased macrophage infiltration ($p = 0.145$). The most predominant immune subtypes before and after treatment was the interferon-γ (IFN-γ)-dominant C2 subtype and the lymphocyte-depleted C4 subtype. Two patients who showed the opposite pattern, transiting from C4 to C2, had durable responses to subsequent atezolizumab/bevacizumab/carboplatin/paclitaxel treatment. Our results shed light on the immunomodulatory effects of osimertinib treatment and suggest that co-targeting angiogenesis and anti-programmed death (ligand) 1 might be effective in EGFR-TKI-resistant non-small cell lung cancer.

INTRODUCTION

Lung cancer is a leading cause of death worldwide, with 85% of cases classified as non-small cell lung cancer (NSCLC), and adenocarcinoma representing the major subtype.[1] Approximately 40–60% of Asian patients with NSCLC exhibit classic-like *EGFR* mutations.[2] Osimertinib, a third-generation EGFR tyrosine kinase inhibitor (TKI), has been shown to improve overall survival in treatment-naïve patients with *EGFR*-mutant advanced/metastatic cancer compared with gefitinib and erlotinib, as evidenced by the FLAURA trial.[3,4] However, most patients eventually develop intrinsic and extrinsic resistance to EGFR-TKIs, necessitating alternative treatment options. Immunotherapies, including immune checkpoint inhibitors (ICIs), have emerged as potent treatment options for patients with advanced cancer.[5,6]

The efficacy of ICIs depends on predictive biomarkers such as programmed death ligand 1 (PD-L1) expression and the tumor mutational burden; however, the overall response rate, ranging from 20% to 40%, mainly due to extrinsic factors associated with the immunosuppressive tumor microenvironment (TME).[7] Specifically, advanced/metastatic *EGFR*-mutant NSCLC often presents with lower TMB and PD-L1 expression,[8] and these tumors are often characterized by low numbers of effector CD8+

T cells and high numbers of regulatory T cells and immunosuppressive cells, such as tumor-associated macrophages and myeloid-derived suppressive cells (MDSCs), which contribute to ICI efficacy.[9–11] Trials combining ICIs to overcome intrinsic resistance have been conducted, including the IMpower150 trial, which used a combination of atezolizumab, bevacizumab, carboplatin, and paclitaxel (ABCP) in patients with *EGFR*-mutant NSCLC following EGFR-TKI failure. The ABCP regimen improved survival outcomes compared with the BCP regimen previously used to treat patients with classic *EGFR*-mutant NSCLC.[12]

EGFR-TKI-treated tumors display increases in effector CD8+ T cell numbers, major histocompatibility complex presentation, and expression of CD8+ T cell recruitment-associated chemokine C-C motif ligand 5 (CCL5) and chemokine C-X-C motif ligand 10 (CXCL10), along with decreased regulatory T cell numbers and chemokine C-C motif ligand 22 (CCL22) expression.[8,9,13] Moreover, EGFR-TKI treatment can modulate M2-polarized macrophages, which are associated with poor survival, into an M1-like phenotype in lung adenocarcinoma.[13,14] The composition of the immune environment changes throughout treatment stages. Before treatment and during disease progression, there is generally low T cell infiltration and a high presence of regulatory T cells; however, when treatment is effective, there

Table 1. Patient demographics of the digital spatial profiling samples

	N (%)
All	25 (100)
Age (years), median (range)	62 (43–79)
Sex	
Male	8 (32)
Female	17 (68)
ECOG performance status	
0	1 (4)
1	23 (92)
2	1 (4)
Smoking history	
Never-smoker	22 (88)
Smoker	3 (12)
EGFR mutation	
L858R	11 (44)
E19del	14 (56)
EGFR-TKIs	
Gefitinib[a]	2 (8)
Osimertinib	23 (92)
PD-L1 (%)	
<1	11 (44)
1–49	5 (20)
≥50	7 (28)
NA	2 (8)
Best response	
PR	24 (96)
PD	1 (4)
Outcome	
Death	17 (68)
AOD	8 (32)
PFS (months), median (range)	16.2 (2.8–35.7)
OS (months), median (range)	34.9 (7.5–127.4)

ECOG, eastern cooperative oncology group; E19del, exon 19 deletion mutation; PR, partial response; PD, progression of disease; AOD, alive on disease; OS, overall survival; PFS, progression-free survival; NA, not available.

[a]One patient was subsequently treated with osimertinib.

is a notable increase in functional T cell infiltration.[15] Considering the preclinical evidence of TME changes following EGFR-TKI treatment, it is crucial to comprehensively understand these changes in a clinical context. In this study, we analyzed the overall TME changes before and after EGFR-TKI treatment using GeoMx digital spatial profiling (DSP).

RESULTS

Patient characteristics and spatial transcriptome profiling

The study cohort included 25 patients, 23 of whom were treated with first-line osimertinib, with the remaining two receiving gefi-
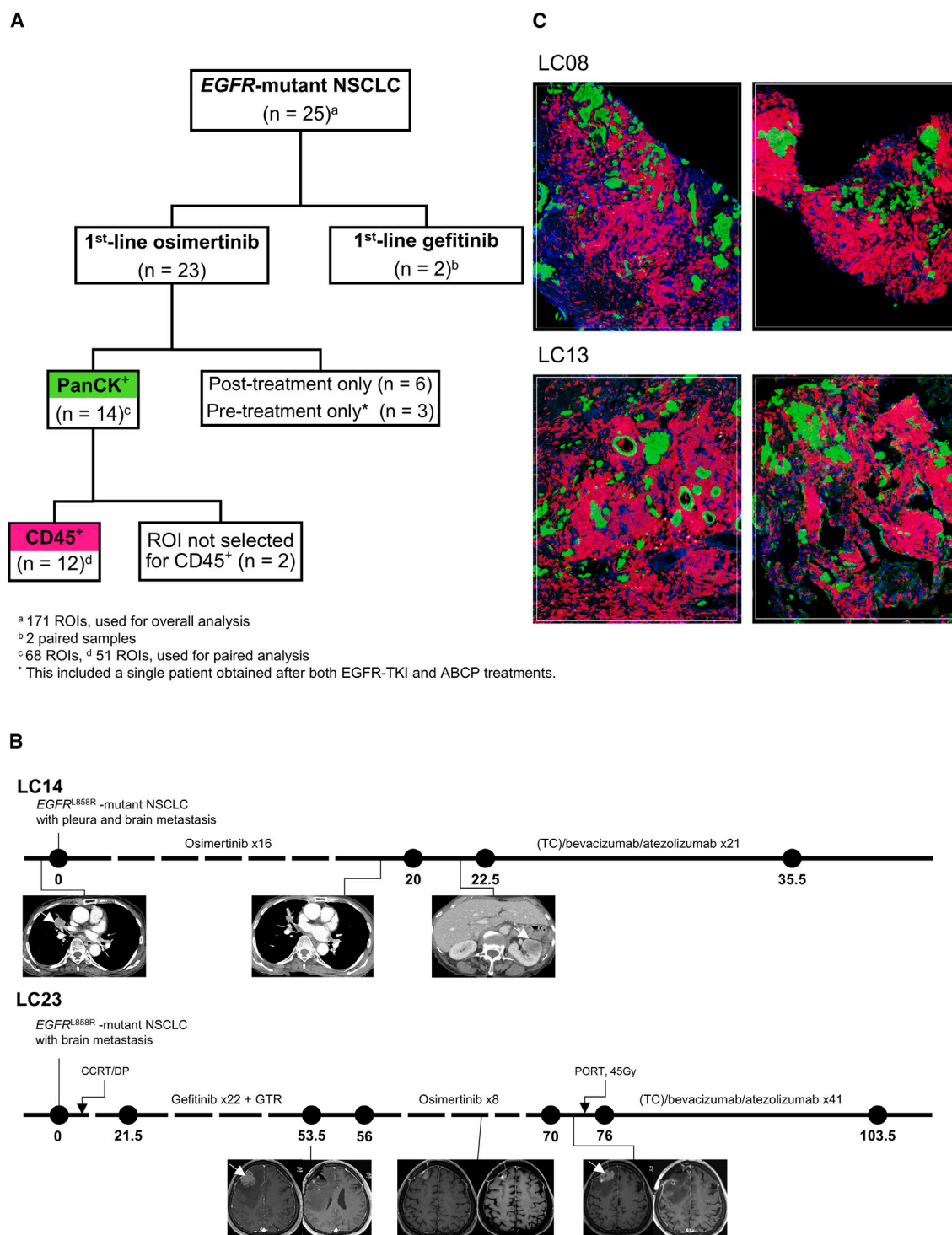
tinib. Eleven patients had *EGFR* L858R mutation, and 14 had an *EGFR* exon 19 deletion. Most patients demonstrated low (<1%, 44% of patients) or moderate (1–49%, 20% of patients) PD-L1 expression. None of the patients displayed well-known mechanisms of acquired resistance to first-line osimertinib, including *EGFR* C797X secondary mutation, *MET* amplification, and transformed small cell carcinoma. Detailed clinical information is presented in Table 1. Overall, 171 regions of interest (ROIs) within the tumors of 25 patients were considered in the DSP analysis. A paired analysis was also conducted using 68 ROIs from the tumors of 14 patients who provided samples both before and after osimertinib treatment. Paired samples without ROIs selected for immune cell infiltration were excluded, resulting in a total of 51 ROIs from 12 patients that were included in the paired analysis of immune regions (Figure 1A). Among these, patients LC14 and LC23 responded favorably to subsequent ABCP treatment and were selected for further analysis (Figure 1B). The selection of ROIs entailed immunostaining of tissue microarrays (TMAs) with specific antibodies targeting CD45 for immune cell demarcation, PanCK for tumor core delineation, and DNA for nuclear staining (Figure 1C). When the cell count exceeded the predefined threshold, a thorough analysis was conducted for each ROI encompassing both PanCK⁺ and CD45⁺ regions.

Whole-transcriptome sequencing was conducted using the NanoString DSP platform, which demonstrated high sequencing saturation and normalization (Figure S1A). A total of 12,356 genes were identified from 173 ROIs using quality control (QC) procedures (Figure S1B). Two ROIs that were obtained after ABCP treatment were excluded from further analysis. Biological probe QC showed sequencing saturation ≥90%, indicating sufficient RNA sequencing coverage. Genes exhibiting expression levels above the limit of quantitation in at least 5% of the analyzed ROIs were selected. Subsequently, Whole-Transcriptome Atlas sequencing data were normalized using third quartile (Q3) expression values, accounting for variations in cellularity and ROI sizes (Figure S1B). The tumor and immune regions were segmented with high precision to ensure reliable outcomes (Figure S1C).

Comparative analysis of differentially expressed genes and pathway alterations

Gene expression levels and associated pathway alterations in immune (CD45⁺) and tumor (PanCK⁺) regions were compared between pre-treatment and post-treatment samples (Figures 2, 3, and S2). Similar patterns were observed in separate analyses of the overall samples and the paired samples, although the magnitudes of change varied.

In the immune regions, 29 and 40 genes were upregulated in the overall pre- and post-treatment samples, and 47 and 72 genes were upregulated in the paired pre- and post-treatment samples, respectively (Figures 2A, 2C, and 2D). Programmed death 1 (PD-1) signaling, the CD28 co-stimulation family, T cell receptor signaling (*cytotoxic T lymphocyte-associated protein 4* [*CTLA4*], *human leukocyte antigen DQB2* [*HLA-DQB2*], *human leukocyte antigen-DQ2A* [*HLA-DQ2A*], and *Enah/VASP-like* [*EVL*]), and the complement cascade (*C3* and *C4B*) were downregulated after EGFR-TKI treatment in both the overall samples and the paired samples (Figures 3A and 3E). Interferon signaling

A

EGFR-mutant NSCLC
(n = 25)[a]

1st-line osimertinib
(n = 23)

1st-line gefitinib
(n = 2)[b]

PanCK+
(n = 14)[c]

Post-treatment only (n = 6)
Pre-treatment only* (n = 3)

CD45+
(n = 12)[d]

ROI not selected
for CD45+ (n = 2)

[a] 171 ROIs, used for overall analysis
[b] 2 paired samples
[c] 68 ROIs, [d] 51 ROIs, used for paired analysis
* This included a single patient obtained after both EGFR-TKI and ABCP treatments.

C

LC08

LC13

B

LC14

EGFR[L858R]-mutant NSCLC
with pleura and brain metastasis

LC23

EGFR[L858R]-mutant NSCLC
with brain metastasis

Figure 1. Sample selection and regions of interest for digital spatial profiling

(A) Patient selection scheme for paired first-line osimertinib-treated samples. *n* refers to the number of patients excluded from the study. PanCK+ denotes tumor regions, and CD45+ denotes immune regions.

(legend continued on next page)

(*HLA-B*, *HLA-C*, *HLA-E*, *HLA-F*, *HLA-DAQ2*, *tripartite motif-containing 2* [*TRIM2*], and *signal transducer and activator of transcription 1* [*STAT1*]) was also decreased after EGFR-TKI treatment (Figures 3A and S2A), which was consistent with findings in the tumor regions. Furthermore, antigen presentation and vascular endothelial growth factor receptor 2 (VEGFR2)-mediated cell proliferation were decreased after osimertinib treatment in the paired samples (Figure 3A). Conversely, expression of genes related to extracellular matrix (ECM) organization (*cathepsin L* [*CTSL*], *integrin beta 3* [*ITGB3*], and *fibulin 1* [*FBLN1*]) and collagen formation (*collagen type V alpha 1* [*COL5A1*] and *peroxidasin* [*PXDN*]) was increased in the paired samples after osimertinib treatment, matching the results in the tumor regions. GSEA revealed a decrease in interferon-gamma signaling after osimertinib treatment (Figure 3B). Moreover, expression of the inflammatory cytokine interleukin-32 (*IL32*) was decreased after EGFR-TKI treatment in the overall samples and the paired samples, and that of *CCL5*, a chemoattractant related to T cell migration and interferon-gamma response, was decreased after osimertinib treatment in the paired samples (Figures 2A and S2A).

In the tumor regions, 44 and 35 genes were upregulated in the overall pre- and post-treatment samples, and 39 and 44 genes were upregulated in the paired pre- and post-treatment samples, respectively (Figures 2B, 2E, and 2F). Pathway analysis of the overall and paired samples revealed that cell-cell junction organization (*Claudin 11* [*CLDN11*]) was downregulated after EGFR-TKI treatment, whereas epigenetic regulatory pathways, including DNA methylation, histone deacetylase (HDAC) deacetylation, and polycomb repressive complex 2 (PRC2) methylation of histones and DNA, were upregulated (Figures 3C and 3F). In addition, the angiogenesis and epithelial-mesenchymal transition (EMT) pathways and genes related to fibroblast and tumor growth, such as *fibroblast growth factor binding protein 1* (*FGFBP1*), *fibroblast growth factor receptor 1* (*FGFR1*), and *neuropilin 2* (*NRP2*) were specifically upregulated after osimertinib treatment in the paired samples (Figure 3D). Furthermore, pathways related to cell motility, promoted by the proto-oncogene and receptor tyrosine kinase MET, and integrin cell surface interactions (*fibronectin 1* [*FN1*], *matrix metalloproteinase 9* [*MMP9*], and *a disintegrin and metalloproteinase 28* [*ADAM28*]) were upregulated after osimertinib treatment in the paired samples, which may have been related to resistance mechanisms (Figures 3C and S2B). Expression of *CCL2*, which is linked to macrophage and MDSC recruitment and humoral response, was also increased after EGFR-TKI treatment (Figures 2B and S2B). Conversely, expression of immunoglobulin genes known to promote tmor growth and enhance metastasis[16] (*Immunoglobulin Kappa Constant* [*IGKG*] and *immunoglobulin heavy constant gamma 3* [*IGHG3*]) was decreased after osimertinib treatment in the paired samples (Figure S2B). There were no significant changes in the kynurenine signature, which is implicated in cancer progression, in the paired samples after osimertinib treatment[15] (Figure 2G). To validate our findings, we analyzed the public Gene Expression Omnibus (GEO): GSE259387[17] dataset and observed increased expression of genes related to angiogenesis (*ephrin B1* [*EFNB1*], *polycystin 1* [*PKD1*], *AKT serine/threonine kinase 3* [*AKT3*], and *APC regulator of WNT signaling pathway 2* [*APC2*]) and ECM (*collagen type V alpha 1* [*COL5A2*], *collagen type XI alpha 2 chain* [*COL11A2*], *collagen type IX alpha 3 chain* [*COL9A3*]) after osimertinib treatment (Figure 2H).

Changes in immune cell composition

We identified 22 immune cell subtypes in the pre- and post-treatment samples using CIBERSORTx. M0, M1, and M2 macrophages were classified as macrophages, naive and memory B cells were classified as B cells, resting and activated natural killer cells were categorized as NK cells, and dendritic cells included both the resting and the activated states (Figures 4 and S4). In the paired samples, the proportion of plasma cells decreased from 22.2% to 11.7% after osimertinib treatment (Figure 4A). Although no statistically significant differences were identified in the overall samples, there was a slight increase in M2 macrophages and a decrease in M1 macrophages after EGFR-TKI treatment (Figure 4B). In the paired samples, immunohistochemistry revealed an increase in CD3+Foxp3+ T cells (*p* = 0.033) and CD68+CD163+ macrophages (*p* = 0.003) in 7 of 11 patients (63.6%), indicating an overall elevation of immunosuppressive immune cells after treatment (Figures 4C and S5). Moreover, in the paired samples, there was an inverse relationship within each patient between the changes in M2 macrophages and the changes in CD8+ T cells following osimertinib treatment (Figure 4D).

With respect to T cells, there were no significant changes in the proportions of CD8+ effector cells, regulatory T cells, or naive T cells after EGFR-TKI treatment in the overall samples (data not shown) (Figure S4); however, in the paired samples, there was an increase in regulatory T cells (CD3+ Foxp3+) after osimertinib treatment (Figures 4B and 4C). Additionally, both the immune score and the microenvironment score declined in the paired samples after osimertinib treatment (Figure 4E). Analysis of immune exhaustion markers revealed a decrease in *CTLA4* after EGFR-TKI treatment in the overall samples, whereas *hepatitis A virus cellular receptor 2* (*HAVRC2*) and *programmed cell death 1* (*PDCD1*) did not show significant changes (Figure 4F). In addition, *indoleamine 2,3-dioxygenase 1* (*IDO1*), a macrophage-associated gene related to progression state,[15] was decreased, whereas *DNA topoisomerase II alpha* (*TOP2A*) was increased, in the post-treatment samples (Figure 4F).

Changes in immune signatures after osimertinib treatment

According to Thorsson's classification of immune signatures,[18] the paired samples displayed several immune subtypes, including

(B) Timeline indicating the time points of tissue acquisition, with white arrows on the images indicating sites from which samples were obtained. The numbers on the timeline represent the number of months since the diagnosis of metastatic NSCLC. Representative tissues from patients LC14 and LC23 are shown. TC, paclitaxel and carboplatin; CCRT/DP, concomitant chemoradiotherapy/docetaxel plus cisplatin; GTR, gross total resection; PORT, post-operative radiotherapy.
(C) Representative region of interest (ROI) images of paired tissue samples from the same patient and tissue origin. Right supraclavicular lymph node (top) and lung (bottom). ROIs were imaged using three fluorescence channels, PanCK (green), DNA (blue), and CD45 (red), to select regions containing both tumor cells and immune cells. Colored regions represent masked regions where RNA was obtained. ROIs 660 μm × 785 μm in size were selected.
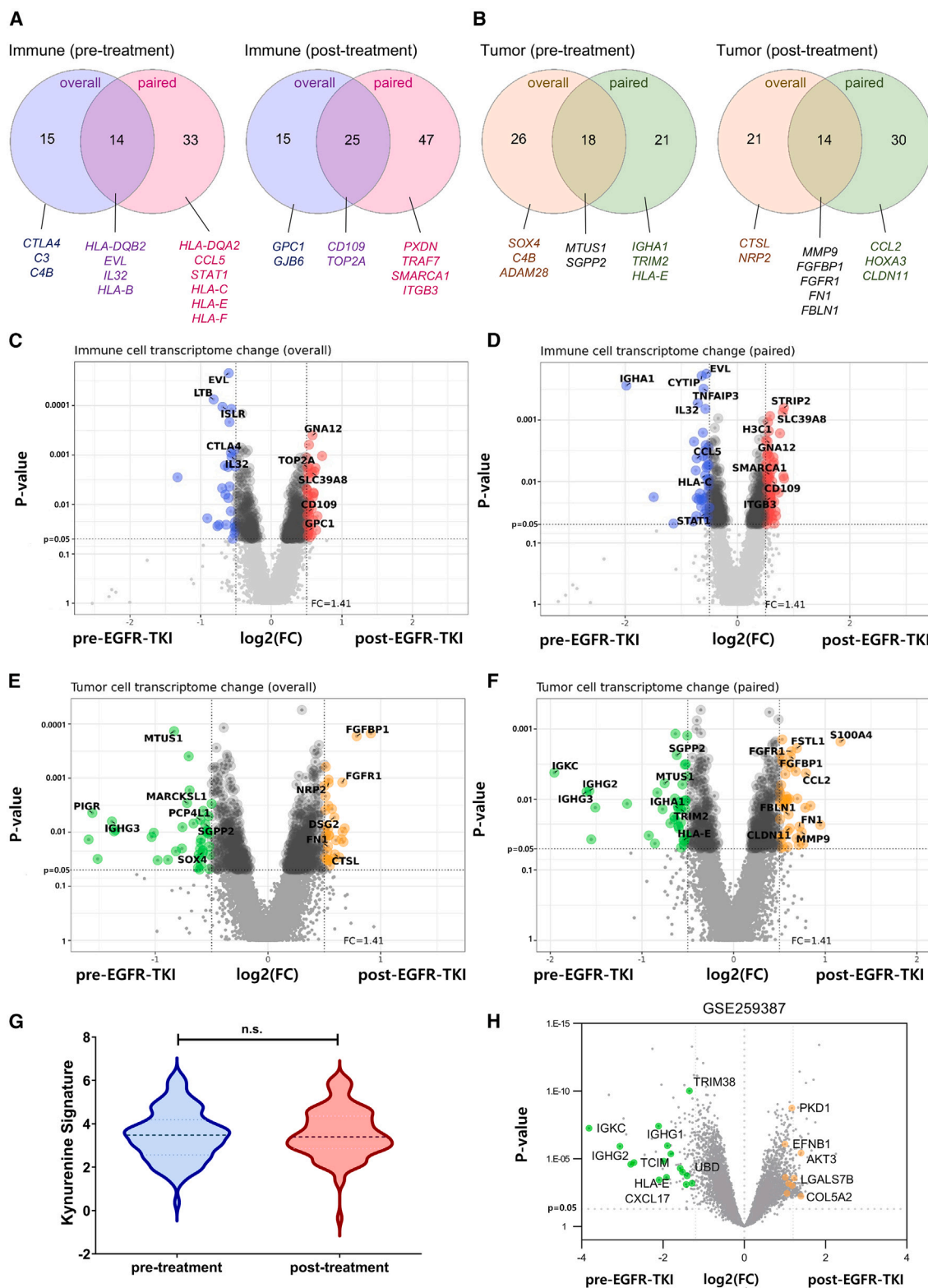
C2 (interferon-γ [IFN-γ] dominant), C3 (inflammatory), C4 (lymphocyte-depleted), and C6 (transforming growth factor β [TGF-β] dominant). Subtypes C1 (wound healing) and C5 (immunologically quiet) were absent from our samples. When the different subtypes were assigned to various ROIs within the same patient, the average probability of each subtype was calculated, and the subtype with the highest average probability was assigned to the patient. When the probabilities of different subtypes were comparable, the two most likely subtypes were represented in a Sankey diagram. When the immune subtypes assigned to each patient before and after osimertinib treatment were considered, the most frequent pattern was C4 to C4 in six patients, followed by C2 to C4 in three patients and C4 to C2 in two patients. Additionally, transitions from C2 to C3, C3 to C4, C6 to C2, and C6 to C4 were observed in one patient each (Figures 5A and S6A). C4 status was confirmed by the combination of *EGFR* overexpression and a higher ratio of M2 macrophages,[18] as illustrated in Figure 5B. This analysis was performed on samples with distinct signatures, irrespective of their pre- or post-treatment status. In instances where subsequent ABCP treatment resulted in a favorable response, as in patients LC14 and LC23 (Figure 1B), an increase in the proportion of immune cells and a decrease in the ratio of M2 macrophages were observed (Figure 5C). Moreover, patients LC14 and LC23, who exhibited prolonged responses to subsequent ABCP treatment, transitioned from the C4 immune subtype to the C2 immune subtype (Figure 5C). Although patient LC14 displayed a significant increase in CD163^{+} macrophages, no such change was observed in patient LC23. In addition, notable increases in CD163^{+} macrophages were observed in patients who showed C4 to C4 transits (patients LC01, LC05, LC16, and LC29).

The seven groups of immunomodulatory genes exhibited different expression patterns among the immune subtypes, with the expression levels of co-stimulatory genes increased in C2 and decreased in C4. The expression levels of inhibitory genes such as *CD274*, *IL13*, *CCL5*, and *CTLA4* and genes related to cytotoxicity, such as *granzyme A* (*GZMA*), *perforin-1* (*PRF1*), *indoleamine-2,3-dioxygenase 1* (*IDO1*), and *CXCL9*, were also higher in C2 compared with C4. Conversely, the expression levels of cell adhesion-related genes were higher in C4 than in C2 (Figure S6B).

DISCUSSION

EGFR-TKIs, which are the standard treatment for classic *EGFR*-mutant NSCLC, can potentially modulate the TME to create a favorable environment for immunotherapy. We used DSP to comprehensively examine TME changes in *EGFR*-mutant NSCLC tumors that previously acquired resistance to EGFR-

TKIs. We found that after EGFR-TKI treatment, interferon, PD-1, and TCR signaling and the CD28 co-stimulation family were downregulated in immune ROIs. These changes may contribute to the development of an immunosuppressive microenvironment that enables tumor immune evasion. Furthermore, we observed upregulation in pathways related to ECM organization, collagen formation, angiogenesis, and EMT, which are known to promote tumor progression and metastasis. These results confirm that acquisition of resistance to EGFR-TKIs led to a more conducive environment for tumor growth.

One notable finding was the significant decrease in immune scores following treatment with first-line osimertinib, indicating reduced infiltration of immune cells into tumor regions.[19] A high immune score is often linked to a favorable prognosis in NSCLC.[20] Additionally, the C6 immune subtype, which was present in some of the patients before osimertinib treatment, was absent in the post-treatment samples, reflecting a decrease in immune cell infiltration. Specifically, after EGFR-TKI treatment, the proportion of plasma cells decreased, whereas the proportion of M2 macrophages increased slightly. This increase in M2 macrophages is associated with higher expression of *CCL2*, a key chemokine responsible for macrophage recruitment.[21] Moreover, M2 macrophages are known to promote tumor progression and resistance by suppressing T cell function and enhancing angiogenesis and EMT.[22] CD68^{+}CD163^{+} macrophages were increased in the post-treatment samples, implying that tumors with acquired resistance to EGFR-TKI treatment had an increased ability to induce regulatory T cells and angiogenesis.[23,24] The negative correlation between M2 macrophages and effector CD8^{+} T cells observed in the paired samples suggests that macrophages could obstruct T cell function.[25] Additionally, M2 macrophages engage in angiogenesis by degrading ECM and fostering endothelial cell growth,[26] a pattern which was noted in our study, underscoring the therapeutic potential of anti-angiogenesis therapy after resistance to EGFR-TKIs develops. Changes in the angiogenesis pathway in tumor regions following treatment with first-line osimertinib provide insight into potential combinations of anti-angiogenesis therapies. These results are consistent with those of a previous study of TME changes that occurred after resistance to second-line osimertinib developed.[27] Conversely, our observations in patient LC14 hint at a more favorable immune response with fewer M2 macrophages for improved ABCP treatment results. Indeed, the observed decrease in plasma cells and concurrent increase in M2 macrophages and regulatory T cells after osimertinib treatment are indicative of an immunosuppressive and less inflammatory TME. In two cases of good responses to immunotherapy in our cohort, the opposite pattern was observed, suggesting a more favorable immune phenotype. However, because we did not compare the effects of ABCP according to

---

Figure 2. Differentially expressed genes between pre- and post-treatment samples
Venn diagrams show differentially expressed genes (DEGs) in the overall and paired samples.
(A and B) Upregulated and downregulated DEGs in the immune (A) and tumor (B) regions, pre-treatment (left) and post-treatment (right). The specific gene names are listed below each plot.
(C–F) Volcano plots illustrating DEGs between pre- and post-treatment samples in the overall immune (C), paired immune (D), overall tumor (E), and paired tumor (F) regions. The dotted lines represent log2 fold change (FC) > 0.4957 or < −0.4957. Labels indicate the selected genes.
(G) Kynurenine pathway score in the paired tumor samples. Data are represented as mean ± SD.
(H) Volcano plot illustrating DEGs between pre- and post-treatment samples in Gene Expression Omnibus (GEO): GSE259387 dataset.
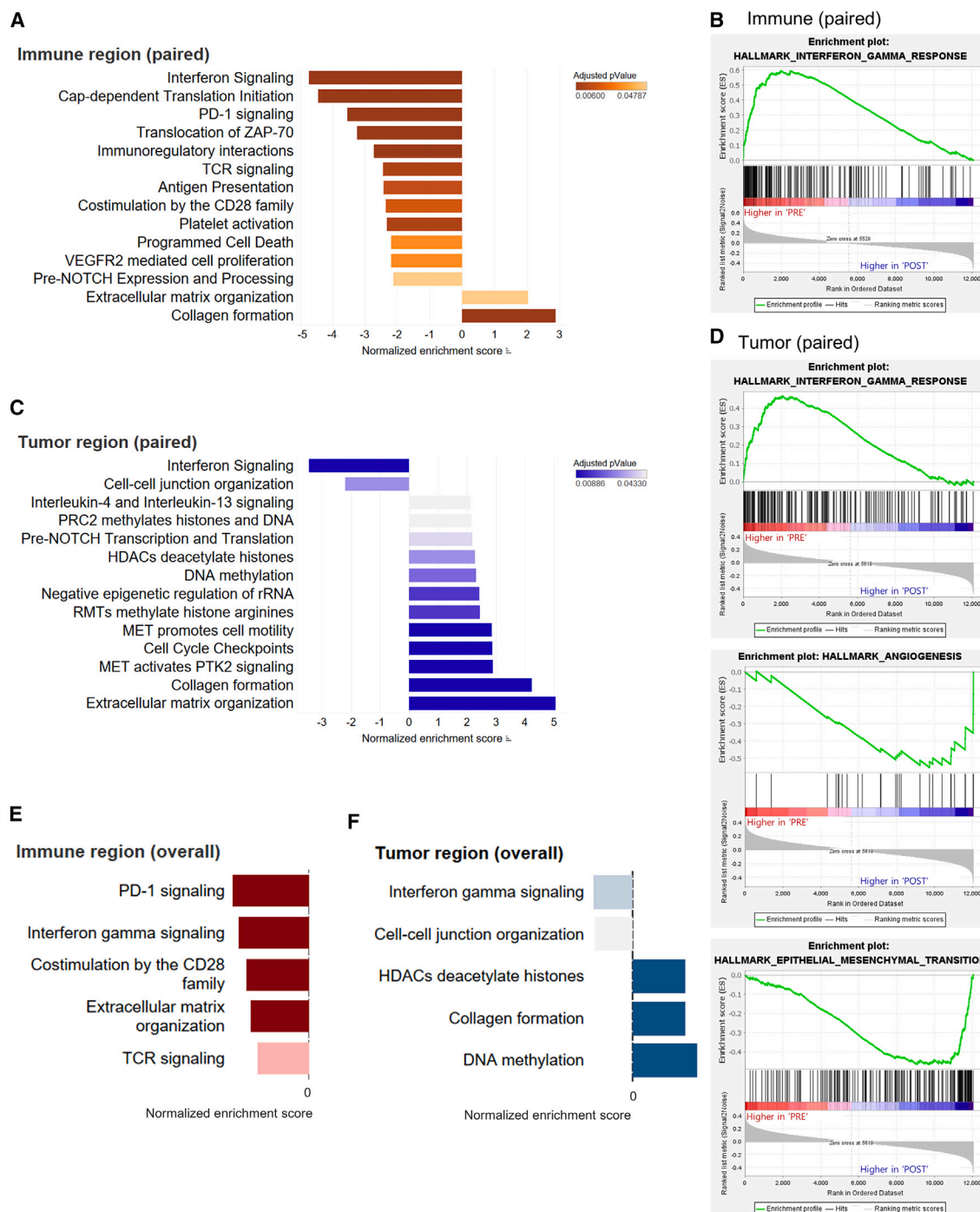
Figure 3. Pathway and gene set enrichment analyses of pre- and post-treatment samples

(A–F) Pathway analyses of the digital spatial profiling samples in the paired immune (A) and tumor (C) regions. Negative normalized enrichment score indicates upregulation in pre-treatment samples, whereas a positive score indicates upregulation in post-treatment samples. These pathways represent the most significantly differentiated pathways between pre- and post-treatment samples (adjusted p value <0.05). Gene set enrichment analysis of transcriptional profiles of paired immune (hallmark interferon-gamma response) (B) and tumor (hallmark interferon-gamma response, hallmark angiogenesis, and hallmark epithelial-mesenchymal transition in paired immune) (D) regions. Positive enrichment score (ES) indicates gene sets enriched in the pre-treatment samples, whereas negative ES indicates gene sets enriched in the post-treatment samples. Normalized ESs of five selected pathways in the overall immune (E) and tumor (F) regions are shown.
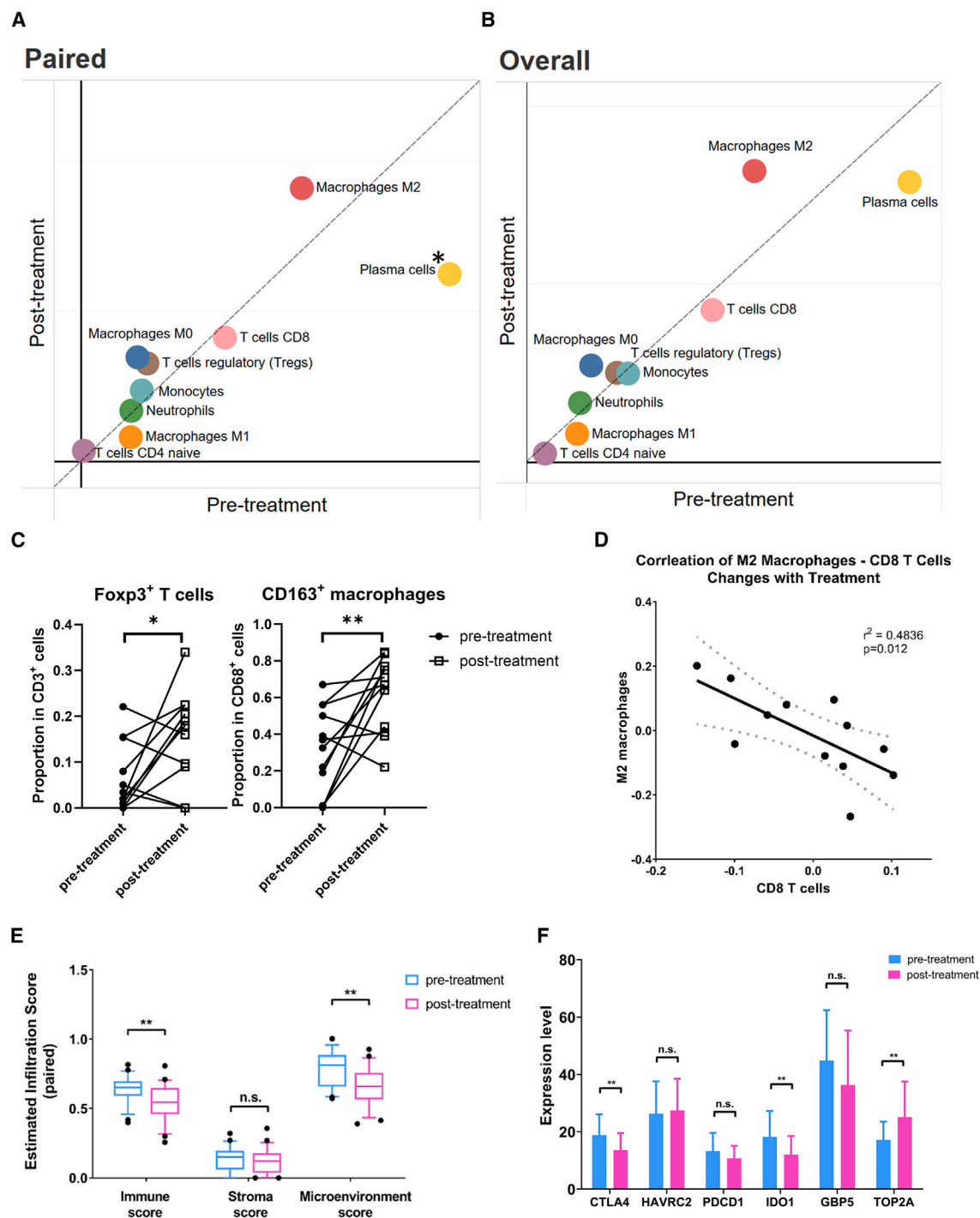
**Figure 4. Comparison of immune environments in the pre- and post-treatment samples**

(A and B) Dot plots of 10 immune subtypes selected from the pre- and post-treatment CIBERSORTx results in the overall (A) and paired (B) samples. Plots above the y = x line indicate a higher post-treatment immune population, whereas plots below indicate a higher pre-treatment immune population.

(C) Immunohistochemistry staining with CD3, CD68, Foxp3, and CD163 markers in paired samples.

(D) Scatter graph showing a negative correlation between CD8$^+$ T cells and M2 macrophages in the paired samples. The R-squared value is 0.4836, and the p value is 0.012.

(E) Box-and-whisker plots of the immune, stromal, and microenvironment scores obtained from xCell.

(F) Boxplot showing a comparison of the expression levels of *CTLA4*, *HAVRC2*, *PDCD1*, *IDO1*, *GBP5*, and *TOP2A*. All data are represented as mean ± SD. n.s., not significant; *, $p < 0.05$; **, $p < 0.01$.
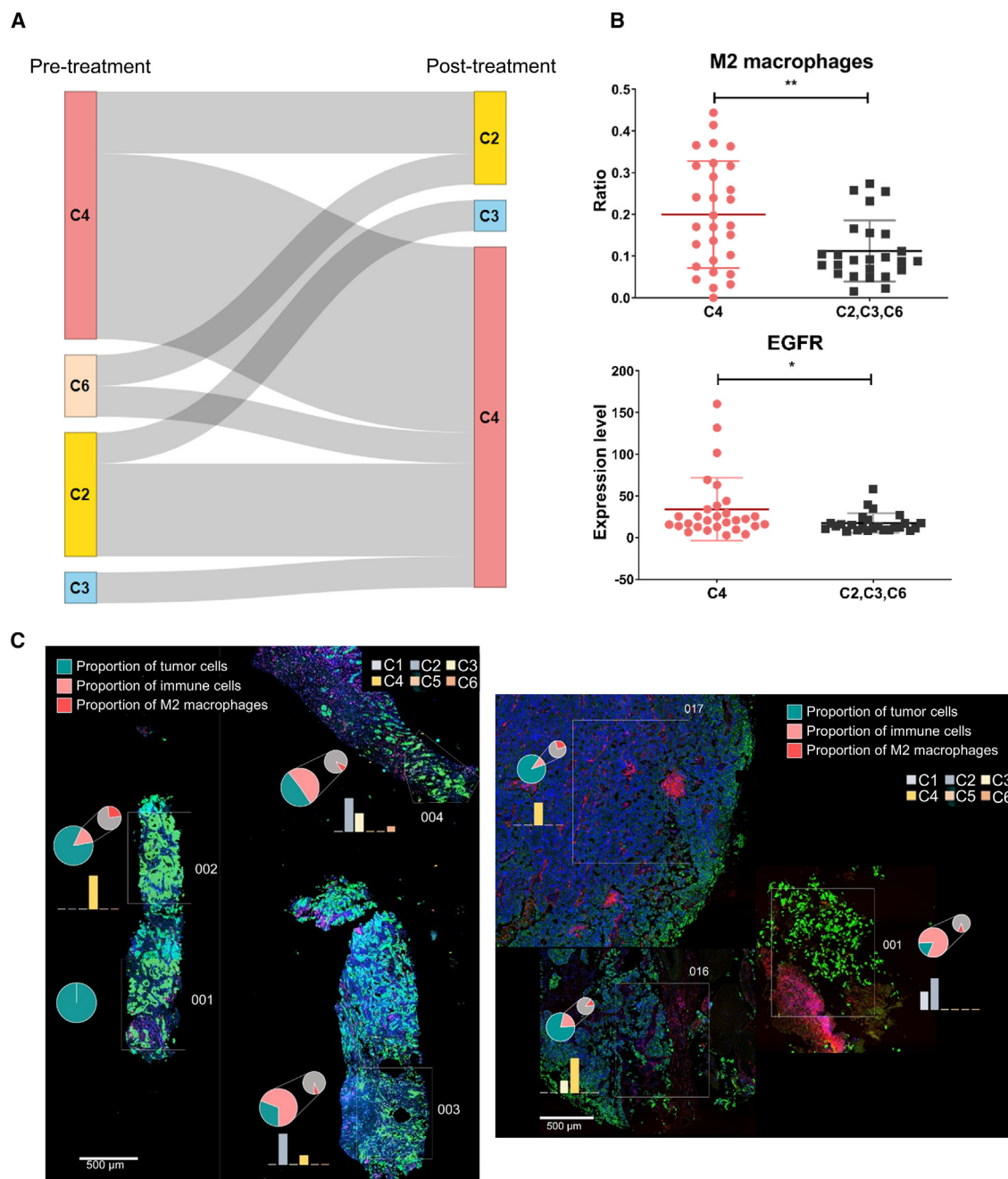
Figure 5. Changes in immune subtypes after treatment

(A) Changes in immune subtype classification in paired pre- and post-treatment samples.

(B) M2 macrophages and *EGFR* levels in the C4 subtype compared with the C2, C3, and C6 subtypes. *, $p < 0.05$. **, $p < 0.01$. Data are represented as mean ± SD.

(C) Digital spatial profiling images of patients LC14 and LC23, and pie charts indicating the proportions of tumor cells, immune cells, and M2 macrophages. Regions of interest (ROIs) 001 and 002 are pre-treatment samples, and ROIs 003 and 004 are post-treatment samples from patient LC14. ROIs 016 and 017 are pre-treatment samples, and ROI 001 is a post-treatment sample for patient LC23. The proportion of each cell type was calculated based on the nuclei count per ROI. The bar graph shows the proportion of C1 versus C6 immune subtypes. Scale bar, 500 μm.

the proportion of M2 macrophages, it is unclear if M2 macrophages affected the treatment efficacy.

We noted changes in the immune signature after osimertinib treatment based on Thorsson's classification.[18] Specifically,

we observed transitions from the more inflammatory C2 subtype to the immunosuppressive C4 subtype in three of 14 patients. The transition to the C4 subtype was associated with an increase in CD163⁺ macrophages, suggesting development of an

immunosuppressive phenotype. Although the C4 subtype was dominant in the post-treatment samples, the specific subtype transits were heterogeneous and unpredictable. Furthermore, patients who exhibited good responses to subsequent ABCP treatment showed an opposite pattern, transiting from the C4 subtype to the C2 subtype. Additionally, the expression levels of immune checkpoint molecules (e.g., *CTLA4* and *PDCD1*) were decreased after osimertinib treatment, suggesting that the TME was likely to be less responsive to checkpoint inhibitors. Moreover, we observed decreases in the expression of inflammatory-related genes, such as *IL32*,[28] and increases in the expression of *CD109*, which is associated with drug resistance.[29] Tumors become more aggressive after they acquire resistance, and the osimertinib-treated samples accordingly displayed increased epigenetic alterations[30] and EMT. The upregulation of collagen formation in the tumor and immune regions, along with ECM reorganization, indicates aggressive tumor behavior, TME alteration, and impeded effector cell infiltration,[31] processes that are linked to the expression of genes such as *FGFBP1*, *FGFR1*, and *NRP2*.[32,33] Overall, the upregulation of specific genes and pathways along with the development of a suppressive immune signature suggests that tumor cells become more aggressive and the TME becomes less inflamed following treatment with osimertinib or other EGFR-TKIs.

Conclusions

This study illustrates changes in the TME following EGFR-TKI treatment in metastatic *EGFR*-mutant NSCLC. Downregulation of immune-related pathways and increases in immunosuppressive cell populations indicate the formation of an immunosuppressive TME. These findings underscore the importance of monitoring TME changes and considering combination therapies, such as anti-angiogenesis therapy, to enhance treatment outcomes. Despite the small sample size, positive responders to ABCP treatment exhibited TME changes that contrasted with those of other patients, highlighting the critical role of the TME in subsequent immunotherapy. Further studies are needed to evaluate immune cell interactions and changes in the tumor compartment related to EGFR-TKI resistance, including angiogenesis, EMT, and FGFR signaling. TME modulation by angiogenesis inhibition and the potential for synergistic effects by co-targeting angiogenesis and PD-(L)1 should be explored further in EGFR-TKI-resistant NSCLC.

Limitations of the study

Because the samples were obtained from different organs, it is important to note that the heterogeneity of our sample limits the generalizability of our findings. In addition, small sample size including a few patients treated with ABCP and limited regional transcriptome without single-cell resolution may weaken the TME remodeling of EGFR-TKI regimen. Further *in vitro* and *in vivo* validation studies should be performed to evaluate the efficacy and TME change of co-targeting PD-(L)1 and angiogenesis against advanced *EGFR*-mutant NSCLC at resistance to EGFR-TKI.

Ethics approval and consent to participate

This study was reviewed and approved by the Institutional Review Board of Seoul National University Hospital (H-2004-056-

1116). Patients treated with first-line osimertinib were registered on clinicaltrials.gov (NCT03969823). Three patients received the ABCP regimen based on the KCSG-LU19-04 trial (NCT039 91403).

AUTHOR CONTRIBUTIONS

Conceptualization: S.K. and T.M.K.; methodology: S.K., J.K., S.O., S.K. and Y.K.J.; investigation: S.K., J.K., T.M.K., and Y.K.J.; writing—original draft: S.K. and T.M.K.; writing—review and editing: J.K., S.O., S.K., J.Y., M.K., B.K., D.-W.K., Y.K.J., and D.S.H.; funding acquisition: T.M.K.; resources: T.M.K., J.Y., M.K., B.K., and D.-W.K.; supervision: T.M.K. and D.S.H.; validation: S.K. and S.O.; formal analysis: S.K., J.K., and S.O.; data curation: S.K. and J.K.

STAR★METHODS

Detailed methods are provided in the online version of this paper and include the following:

- KEY RESOURCES TABLE
- EXPERIMENTAL MODEL AND STUDY PARTICIPANT DETAILS
  - Collection of tumor samples from patients with NSCLC
  - Ethical approval and study registration
- METHOD DETAILS
  - Digital spatial profiling
  - Immunohistochemistry (IHC)
- QUANTIFICATION AND STATISTICAL ANALYSES

REFERENCES

1. Thai, A.A., Solomon, B.J., Sequist, L.V., Gainor, J.F., and Heist, R.S. (2021). Lung cancer. Lancet *398*, 535–554. https://doi.org/10.1016/s0140-6736(21)00312-3.

2. Tan, A.C., and Tan, D.S.W. (2022). Targeted Therapies for Lung Cancer Patients With Oncogenic Driver Molecular Alterations. J. Clin. Oncol. *40*, 611–625. https://doi.org/10.1200/jco.21.01626.

3. Soria, J.-C., Ohe, Y., Vansteenkiste, J., Reungwetwattana, T., Chewaskulyong, B., Lee, K.H., Dechaphunkul, A., Imamura, F., Nogami, N., Kurata, T., et al. (2018). Osimertinib in Untreated EGFR-Mutated Advanced Non–Small-Cell Lung Cancer. N. Engl. J. Med. *378*, 113–125. https://doi.org/10.1056/NEJMoa1713137.

4. Ramalingam, S.S., Vansteenkiste, J., Planchard, D., Cho, B.C., Gray, J.E., Ohe, Y., Zhou, C., Reungwetwattana, T., Cheng, Y., Chewaskulyong, B., et al. (2020). Overall Survival with Osimertinib in Untreated, EGFR-Mutated Advanced NSCLC. N. Engl. J. Med. *382*, 41–50. https://doi.org/10.1056/NEJMoa1913662.

5. Passaro, A., Jänne, P.A., Mok, T., and Peters, S. (2021). Overcoming therapy resistance in EGFR-mutant lung cancer. Nat. Cancer *2*, 377–391. https://doi.org/10.1038/s43018-021-00195-8.

6. Chen, Y., Chen, Z., Chen, R., Fang, C., Zhang, C., Ji, M., and Yang, X. (2022). Immunotherapy-based combination strategies for treatment of EGFR-TKI-resistant non-small-cell lung cancer. Future Oncol. *18*, 1757–1775. https://doi.org/10.2217/fon-2021-0862.

7. Hastings, K., Yu, H.A., Wei, W., Sanchez-Vega, F., DeVeaux, M., Choi, J., Rizvi, H., Lisberg, A., Truini, A., Lydon, C.A., et al. (2019). EGFR mutation subtypes and response to immune checkpoint blockade treatment in non-small-cell lung cancer. Ann. Oncol. *30*, 1311–1320. https://doi.org/10.1093/annonc/mdz141.

8. Sugiyama, E., Togashi, Y., Takeuchi, Y., Shinya, S., Tada, Y., Kataoka, K., Tane, K., Sato, E., Ishii, G., Goto, K., et al. (2020). Blockade of EGFR improves responsiveness to PD-1 blockade in EGFR-mutated non–small cell lung cancer. Sci. Immunol. *5*, eaav3937. https://doi.org/10.1126/sciimmunol.aav3937.

9. Madeddu, C., Donisi, C., Liscia, N., Lai, E., Scartozzi, M., and Macciò, A. (2022). EGFR-Mutated Non-Small Cell Lung Cancer and Resistance to Immunotherapy: Role of the Tumor Microenvironment. Int. J. Mol. Sci. *23*, 6489.

10. Kumagai, S., Koyama, S., and Nishikawa, H. (2021). Antitumour immunity regulated by aberrant ERBB family signalling. Nat. Rev. Cancer *21*, 181–197. https://doi.org/10.1038/s41568-020-00322-0.

11. Yang, L., He, Y.-T., Dong, S., Wei, X.-W., Chen, Z.-H., Zhang, B., Chen, W.-D., Yang, X.-R., Wang, F., Shang, X.-M., et al. (2022). Single-cell transcriptome analysis revealed a suppressive tumor immune microenvironment in EGFR mutant lung adenocarcinoma. J. Immunother. Cancer *10*, e003534. https://doi.org/10.1136/jitc-2021-003534.

12. Nogami, N., Barlesi, F., Socinski, M.A., Reck, M., Thomas, C.A., Cappuzzo, F., Mok, T.S.K., Finley, G., Aerts, J.G., Orlandi, F., et al. (2022). IMpower150 Final Exploratory Analyses for Atezolizumab Plus Bevacizumab and Chemotherapy in Key NSCLC Patient Subgroups With EGFR Mutations or Metastases in the Liver or Brain. J. Thorac. Oncol. *17*, 309–323. https://doi.org/10.1016/j.jtho.2021.09.014.

13. Isomoto, K., Haratani, K., Hayashi, H., Shimizu, S., Tomida, S., Niwa, T., Yokoyama, T., Fukuda, Y., Chiba, Y., Kato, R., et al. (2020). Impact of EGFR-TKI Treatment on the Tumor Immune Microenvironment in EGFR Mutation–Positive Non–Small Cell Lung Cancer. Clin. Cancer Res. *26*, 2037–2046. https://doi.org/10.1158/1078-0432.Ccr-19-2027.

14. Zhang, B., Zhang, Y., Zhao, J., Wang, Z., Wu, T., Ou, W., Wang, J., Yang, B., Zhao, Y., Rao, Z., and Gao, J. (2014). M2-polarized macrophages contribute to the decreased sensitivity of EGFR-TKIs treatment in patients with advanced lung adenocarcinoma. Med. Oncol. *31*, 127. https://doi.org/10.1007/s12032-014-0127-0.

15. Maynard, A., McCoach, C.E., Rotow, J.K., Harris, L., Haderk, F., Kerr, D.L., Yu, E.A., Schenk, E.L., Tan, W., Zee, A., et al. (2020). Therapy-Induced Evolution of Human Lung Cancer Revealed by Single-Cell RNA Sequencing. Cell *182*, 1232–1251.e22. https://doi.org/10.1016/j.cell.2020.07.017.

16. Jiang, C., Huang, T., Wang, Y., Huang, G., Wan, X., and Gu, J. (2014). Immunoglobulin G expression in lung cancer and its effects on metastasis. PLoS One *9*, e97359. https://doi.org/10.1371/journal.pone.0097359.

17. Oh, S., Koh, J., Kim, T.M., Kim, S., Youk, J., Kim, M., Keam, B., Jeon, Y.K., Ku, J.-L., Kim, D.-W., et al. (2024). Transcriptomic heterogeneity of EGFR-mutant non-small cell lung cancer evolution towards small cell lung cancer. Clin. Cancer Res. *30*, 4729–4742. https://doi.org/10.1158/1078-0432.Ccr-24-0160.

18. Thorsson, V., Gibbs, D.L., Brown, S.D., Wolf, D., Bortone, D.S., Ou Yang, T.H., Porta-Pardo, E., Gao, G.F., Plaisier, C.L., Eddy, J.A., et al. (2018). The Immune Landscape of Cancer. Immunity *48*, 812–830.e14. https://doi.org/10.1016/j.immuni.2018.03.023.

19. Aran, D., Hu, Z., and Butte, A.J. (2017). xCell: digitally portraying the tissue cellular heterogeneity landscape. Genome Biol. *18*, 220. https://doi.org/10.1186/s13059-017-1349-1.

20. Shan, Q., Zhang, Y., and Liang, Z. (2022). Clustering analysis and prognostic signature of lung adenocarcinoma based on the tumor microenvironment. Sci. Rep. *12*, 12059. https://doi.org/10.1038/s41598-022-15971-4.

21. Yang, H., Zhang, Q., Xu, M., Wang, L., Chen, X., Feng, Y., Li, Y., Zhang, X., Cui, W., and Jia, X. (2020). CCL2-CCR2 axis recruits tumor associated macrophages to induce immune evasion through PD-1 signaling in esophageal carcinogenesis. Mol. Cancer *19*, 41. https://doi.org/10.1186/s12943-020-01165-x.

22. Sumitomo, R., Hirai, T., Fujita, M., Murakami, H., Otake, Y., and Huang, C.-L. (2019). M2 tumor-associated macrophages promote tumor progression in non-small-cell lung cancer. Exp. Ther. Med. *18*, 4490–4498. https://doi.org/10.3892/etm.2019.8068.

23. Hwang, I., Kim, J.W., Ylaya, K., Chung, E.J., Kitano, H., Perry, C., Hanaoka, J., Fukuoka, J., Chung, J.Y., and Hewitt, S.M. (2020). Tumor-associated macrophage, angiogenesis and lymphangiogenesis markers predict prognosis of non-small cell lung cancer patients. J. Transl. Med. *18*, 443. https://doi.org/10.1186/s12967-020-02618-z.

24. Ma, X., Gao, Y., Chen, Y., Liu, J., Yang, C., Bao, C., Wang, Y., Feng, Y., Song, X., and Qiao, S. (2021). M2-Type Macrophages Induce Tregs Generation by Activating the TGF-β/Smad Signalling Pathway to Promote Colorectal Cancer Development. OncoTargets Ther. *14*, 5391–5402. https://doi.org/10.2147/ott.S336548.

25. DeNardo, D.G., and Ruffell, B. (2019). Macrophages as regulators of tumour immunity and immunotherapy. Nat. Rev. Immunol. *19*, 369–382. https://doi.org/10.1038/s41577-019-0127-6.

26. Jetten, N., Verbruggen, S., Gijbels, M.J., Post, M.J., De Winther, M.P.J., and Donners, M.M.P.C. (2014). Anti-inflammatory M2, but not pro-inflammatory M1 macrophages promote angiogenesis in vivo. Angiogenesis *17*, 109–118. https://doi.org/10.1007/s10456-013-9381-6.

27. Han, R., Guo, H., Shi, J., Wang, H., Zhao, S., Jia, Y., Liu, X., Li, J., Cheng, L., Zhao, C., et al. (2023). Tumour microenvironment changes after osimertinib treatment resistance in non-small cell lung cancer. Eur. J. Cancer *189*, 112919. https://doi.org/10.1016/j.ejca.2023.05.007.

28. Sloot, Y.J.E., Smit, J.W., Joosten, L.A.B., and Netea-Maier, R.T. (2018). Insights into the role of IL-32 in cancer. Semin. Immunol. *38*, 24–32. https://doi.org/10.1016/j.smim.2018.03.004.

29. Lee, K.Y., Shueng, P.W., Chou, C.M., Lin, B.X., Lin, M.H., Kuo, D.Y., Tsai, I.L., Wu, S.M., and Lin, C.W. (2020). Elevation of CD109 promotes metastasis and drug resistance in lung cancer via activation of EGFR-AKT-mTOR signaling. Cancer Sci. *111*, 1652–1662. https://doi.org/10.1111/cas.14373.

30. Brancolini, C., Gagliano, T., and Minisini, M. (2022). HDACs and the epigenetic plasticity of cancer cells: Target the complexity. Pharmacol. Ther. *238*, 108190. https://doi.org/10.1016/j.pharmthera.2022.108190.

31. Winkler, J., Abisoye-Ogunniyan, A., Metcalf, K.J., and Werb, Z. (2020). Concepts of extracellular matrix remodelling in tumour progression and metastasis. Nat. Commun. *11*, 5120. https://doi.org/10.1038/s41467-020-18794-x.

32. Zhang, Z., Qin, Y., Ji, S., Xu, W., Liu, M., Hu, Q., Ye, Z., Fan, G., Yu, X., Liu, W., and Xu, X. (2021). FGFBP1-mediated crosstalk between fibroblasts and pancreatic cancer cells via FGF22/FGFR2 promotes invasion and metastasis of pancreatic cancer. Acta Biochim. Biophys. Sin. *53*, 997–1008. https://doi.org/10.1093/abbs/gmab074.

33. Islam, R., Mishra, J., Bodas, S., Bhattacharya, S., Batra, S.K., Dutta, S., and Datta, K. (2022). Role of Neuropilin-2-mediated signaling axis in cancer progression and therapy resistance. Cancer Metastasis Rev. *41*, 771–787. https://doi.org/10.1007/s10555-022-10048-0.

34. Heberle, H., Meirelles, G.V., da Silva, F.R., Telles, G.P., and Minghim, R. (2015). InteractiVenn: a web-based tool for the analysis of sets through Venn diagrams. BMC Bioinf. *16*, 169. https://doi.org/10.1186/s12859-015-0611-3.

35. Newman, A.M., Liu, C.L., Green, M.R., Gentles, A.J., Feng, W., Xu, Y., Hoang, C.D., Diehn, M., and Alizadeh, A.A. (2015). Robust enumeration of cell subsets from tissue expression profiles. Nat. Methods *12*, 453–457. https://doi.org/10.1038/nmeth.3337.

36. Reck, M., Mok, T.S.K., Nishio, M., Jotte, R.M., Cappuzzo, F., Orlandi, F., Stroyakovskiy, D., Nogami, N., Rodríguez-Abreu, D., Moro-Sibilot, D., et al. (2019). Atezolizumab plus bevacizumab and chemotherapy in non-small-cell lung cancer (IMpower150): key subgroup analyses of patients with EGFR mutations or baseline liver metastases in a randomised, open-label phase 3 trial. Lancet Respir. Med. *7*, 387–401. https://doi.org/10.1016/S2213-2600(19)30084-0.

37. Merritt, C.R., Ong, G.T., Church, S., Barker, K., Geiss, G., Hoang, M., Jung, J., Liang, Y., McKay-Fleisch, J., Nguyen, K., et al. (2019). High multiplex, digital spatial profiling of proteins and RNA in fixed tissue using genomic detection methods. Preprint at bioRxiv. https://doi.org/10.1101/559021.

STAR★METHODS

KEY RESOURCES TABLE

REAGENT or RESOURCE	SOURCE	IDENTIFIER
Antibodies		
CD3	Ventana Medical Systems	Cat no. 790-4341;RRID: AB_2335978
CD68	DAKO	Cat no. M0814;RRID: AB_2314148
CD163	Cell Marque	Cat no.163M-14;RRID: AB_1159110
Foxp3	Abcam	Cat no. ab20034;RRID: AB_445284
Deposited data		
Nanostring GeoMx DSP data	National Center for Biotechnology Information (NCBI) (https://www.ncbi.nlm.nih.gov)	Gene Expression Omnibus (GEO): GSE285298
Software and algorithms		
GeoMx Digital Spatial Profiler	Nanostring	RRID:SCR_021660
InteractiVenn	Heberle et al.[34]	https://doi.org/10.1186/s12859-015-0611-3
R (v4.2.2)	Rstudio	https://cran.r-project.org/
Prism (v8.0.2)	GraphPad	RRID:SCR_002798
Tableau Desktop (v2023.2.0)	Salesforce	RRID:SCR_013994
CIBERSORTx	Newman et al.[35]	https://cibersortx.stanford.edu/
xCell	Aran et al.	https://comphealth.ucsf.edu/
Other		
Automated staining processor	Ventana Medical Systems Inc.	Benchmark XT
Aperio ScanScope	Aperio Technologies	RRID:SCR_018457

EXPERIMENTAL MODEL AND STUDY PARTICIPANT DETAILS

Collection of tumor samples from patients with NSCLC

The DSP study included 25 Korean patients diagnosed with NSCLC harboring common *EGFR* mutations (L858R and exon 19 micro-deletion) that received EGFR-TKI treatment. Detailed information is listed in Table S1. Sex and gender were not specifically analyzed in this study. Due to the small sample size, data were not stratified by these factors, which may limit the generalizability of the findings. Further studies with larger sample sizes are needed to assess their impact. The sites from which pre- and post-treatment samples were obtained are listed in Table S2. Because of the small sample size, the analysis excluded patients with two ROIs who received ABCP treatment. Among the 25 patients, 16 had paired samples taken before and after EGFR-TKI treatment, whereas 6 only had samples taken after EGFR-TKI treatment, and three only had samples taken before EGFR-TKI treatment. One patient received both osimertinib and ABCP treatment and was excluded from the analysis. Among the 16 sets of paired samples, two were from patients treated with first-line gefitinib (LC23 and LC24) and were excluded from the paired first-line osimertinib group. Thus, 25 patients were analyzed overall, and 14 patients were analyzed in the paired analysis.

Samples were allocated to experimental groups based on treatment regimens and availability of paired pre- and post-treatment samples. Patients were categorized into groups receiving first-line osimertinib or ABCP regimens, and subgroup analyses were conducted separately for tumor and immune regions. Paired analyses included 14 patients for tumor regions and 12 patients for immune regions, reflecting the availability and quality of the corresponding sample sets. The exclusion criteria were applied to ensure the consistency of treatment regimens and the reliability of paired sample data.

Ethical approval and study registration

The study was reviewed and approved by the Institutional Review Board of Seoul National University Hospital (H-2004-056-1116), and written informed consent was obtained from all participants prior to sample collection. Patients treated with first-line osimertinib were registered on clinicaltrials.gov (NCT03969823), and three patients received the ABCP regimen based on the IMpower150 study.[36]

METHOD DETAILS

Digital spatial profiling

TMA slides were prepared according to the GeoMx DSP slide preparation user manual (MAN-10087-04). The overall DSP workflow followed the Nanostring Technologies protocol[37] and can be summarized into five steps: standard formalin-fixed paraffin-embedded tissue preparation, tissue incubation with visualization markers and DSP probes, imaging and ROI selection, ultraviolet exposure, and oligo collection. Visualization markers included three-color fluorescence imaging of epithelial cells (pan-cytokeratin [PanCK, KRT8]), immune cells (CD45 [PTPRC]), and nuclear staining (DNA). One ROI with highly infiltrated immune regions and a maximum size of 660 μm × 785 μm was selected per TMA core based on consultation with experienced pathologists (J.K. and Y.K.J.). Next, the ROIs were exposed to ultraviolet (UV) light to induce cleavage of the linker and to obtain unique barcode oligos from the PanCK$^+$ and CD45$^+$ regions. These barcode oligos were captured using microfluidics and transferred to individual wells of microtiter plates. Gene expression was quantified by digital counting using an nCounter to generate the Whole-Transcriptome Atlas.

Immunohistochemistry (IHC)

The TMA block was sectioned at 4.0 μm thickness. The monoclonal antibodies used for the IHC were CD3 (Ventana, clone 2GV6, Rabbit, monoclonal, RTU), CD68 (DAKO, clone KP1, Mouse, monoclonal, concentration: 1:2,000), CD163 (Cell Marque, clone MRQ-26, Mouse, monoclonal, concentration: 1:200), and Foxp3 (Abcam, clone 236A/E7, Mouse, monoclonal, concentration: 1:100). Immunohistochemistry was performed using the Benchmark XT autostainer (Ventana Medical Systems). Whole-slide images were obtained by virtual microscope scanning of immunohistochemical slides using Aperio ScanScope (Aperio Technologies, Vista, CA, USA). The numbers of CD3$^-$, CD68$^-$, Foxp3-, and CD163-positive cells in each representative 200× magnification field were calculated by a pathologist in a blind manner. We calculated the proportion of Foxp3-positive regulatory T cells within the total CD3$^+$ T cell population, and the proportion of CD163-positive macrophages within the CD68-positive macrophage population.

QUANTIFICATION AND STATISTICAL ANALYSES

For Nanostring, we strictly followed the manufacturer's guidelines and implemented multiple QC measures to maintain data integrity. Technical QC involved flagging segments with <1,000 raw reads; <80% alignment of raw reads; sequencing saturation <50%; negative probe count geomean <10; no template control count >1,000; and minimum surface area <16,000 μm^2. Biological probe QC excluded probes from the target count calculation if the ratio of probe count geomean in all segments to geomean probe count within the target was ≤0.1, and if the grubs outlier test failed in ≥20% of the segments. Following this process, we retained 12,070 biological probes to set a marginal threshold of target frequency >5%. Subsequently, we normalized the data using third quartile normalization and conducted statistical analyses using unpaired t-tests to compare groups based on treatment state within the specified ROIs using GeoMx DSP data analysis software. The ROIs were categorized according to each patient, tumor or immune compartment, and treatment status. We selected ROIs included in each group (overall and paired) and normalized these for each group. Q3 normalization files were used for subsequent analysis.

ROIs for tumor and immune regions were delineated under normalized conditions. Statistical analysis compared DEGs in tumor and immune regions based on treatment state using non-paired t-tests. Samples from each treatment group were analyzed as a single group to allow an overview of the overall trends. Venn diagrams were generated to compare DEGs between groups using InteractiVenn.[34] Volcano plots were created using the Labeled Volcano Plot DSP DA script (v1.2) with the criteria of |log2FC| > 1.41 and $p < 0.05$ based on data obtained from the NanoString platform. Pathway analysis was conducted using the NanoString platform, and data were selected based on an adjusted p-value <0.05. The gene expression dataset GSE259387 was obtained from the Gene Expression Omnibus repository, and additional analyses were performed using this dataset. Data visualization was performed using R (v4.2.2), GraphPad Prism (v8.0.2), and Tableau Desktop (v2023.2.0). Immune signatures were calculated based on a previous study.[18] C4 (lymphocyte-depleted) and C6 (TGF-β dominant) subtypes were characterized by a macrophage-dominated and immunosuppressive microenvironment. C2 (IFN-γ dominant) and C3 (inflammatory) subtypes were associated with a dominant type I immune response. An algorithm available as an open-source package on GitHub (https://github.com/CRI-iAtlas) was used to classify each immune subtype. The proportions of each immune subtype for each ROI were obtained using this algorithm. By analyzing the average values of pre- and post-treatment samples from a single patient, the most dominant subtype was determined. The CIBERSORTx tool, which utilizes a validated leukocyte gene signature matrix (LM22),[35] was used to deconvolute the expression matrix into 22 distinct immune cell subtypes. xCell (https://comphealth.ucsf.edu/), a reliable gene signature-based method for distinguishing each cell subtype, was used to calculate the estimated infiltration scores of 64 immune and stroma cell types in the RNA data using the GSEA algorithm.[19] GSEA (v4.3.2) was used to define the specifically enriched pathways. A Sankey diagram was generated using the networkD3 package (v0.4) in R (v4.2.2). A heatmap was drawn using the R package ComplexHeatmap (v2.14.0), and k-means clustering was performed to classify the samples according to their similarities. All data are presented as the mean ± standard deviation.